Riemann-Encircling Exceptional Points for Efficient Asymmetric Polarization-Locked Devices

Aodong Li,[1,*] Weijin Chen,[2,*] Heng Wei,[2] Guowei Lu,[3] Andrea Alù,[4,5] Cheng-Wei Qiu,[2] and Lin Chen[1,3,†]
[1]Wuhan National Laboratory for Optoelectronics and School of Optical and Electronic Information, Huazhong University of Science and Technology, Wuhan 430074, China
[2]Department of Electrical and Computer Engineering, National University of Singapore, Singapore 117583, Singapore
[3]State Key Laboratory for Mesoscopic Physics, School of Physics, Peking University, Beijing 100871, China
[4]Photonics Initiative, Advanced Science Research Center, City University of New York, New York, New York 10031, USA
[5]Physics Program, Graduate Center, City University of New York, New York, New York 10016, USA

(Received 23 February 2022; accepted 22 August 2022; published 13 September 2022; corrected 20 September 2022)

Dynamically encircling exceptional points (EPs) have unveiled intriguing chiral dynamics in photonics. However, the traditional approach based on an open manifold of Hamiltonian parameter space fails to explore trajectories that pass through an infinite boundary. Here, by mapping the full parameter space onto a closed manifold of the Riemann sphere, we introduce a framework to describe encircling-EP loops. We demonstrate that an encircling trajectory crossing the north vertex can realize near-unity asymmetric transmission. An efficient gain-free, broadband asymmetric polarization-locked device is realized by mapping the encircling path onto L-shaped silicon waveguides.

DOI: 10.1103/PhysRevLett.129.127401

In a non-Hermitian system obeying parity-time (PT) symmetry, two or more eigenvalues and eigenstates are simultaneously degenerate at exceptional points (EPs). A variety of intriguing phenomena, such as sensing enhancement [1–3], unidirectional invisibility [4,5], topological light control [6,7], and asymmetric mode conversion [8–15] have been demonstrated at these singularities, closely linked to their topological features, and they have attracted a growing interest in optics [1,7,8,16–26], acoustics [27–29], thermodynamics [30], electronics [31,32], and quantum mechanics [33].

When a Hamiltonian adiabatically encircles an EP twice, the Berry phase is π, indicating a self-intersecting Riemann surface (RSU) around the EP [34]. Recent studies have demonstrated that this feature enables a chiral response: by dynamically encircling an EP in clockwise (CW) or anticlockwise (ACW) direction leads to different final states, regardless of the starting states. Such chiral response has been demonstrated by mapping the required Hamiltonian parameters onto PT symmetric arrangements of waveguides [8,20,35]. Most previous studies have been applying this feature to realize asymmetric conversion of modes in optical waveguides, but they failed to achieve high transmission efficiencies due to path-dependent loss [8,12,13,20,36,37]. The reason is that the traditional approach to EP encircling is based on an open manifold in the Hamiltonian parameter space. Such approach neglects a set of loops passing through the infinite boundary, enabling low path-dependent losses. Because of significant challenges in practical experimental implementations, high-efficiency polarization-locked device has not been achieved to date [10,38].

In this Letter, we demonstrate that the full Hamiltonian parameter space can be mapped onto the Riemann sphere (RSP), over which infinite points lying on its boundary are associated with the same eigenstates and converge to the north vertex. Benefitting from the RSP mapping, we can encircle an EP along a continuous and closed trajectory passing through the north vertex and achieve highly efficient asymmetric transmission. We present experimental results mapping this trajectory onto L-shaped waveguides, demonstrating near-unity asymmetric conversion efficiency at 1550 nm. Such a functionality corresponds to an asymmetric polarization-locked device (APLD), since the output polarization state is locked irrespective of the input polarization states [39].

A system state $|\psi\rangle$ propagating along z follows a Schrödinger-type equation $i\partial/\partial z|\psi\rangle = H|\psi\rangle$, with second-order Hamiltonian

$$H = \begin{bmatrix} \beta & \kappa \\ \kappa & -\beta - i\gamma \end{bmatrix}, \tag{1}$$

where β, γ, and κ represent the detuning, relative gain or loss rate and coupling strength of the system, respectively. The two eigenvalues are $E_{1,2} = -i\gamma/2 \pm \sqrt{\kappa^2 + (\beta + i\gamma/2)^2}$ and the associated eigenstates are $|\psi_{1,2}\rangle = [\sqrt{1 \pm K}, \pm\sqrt{1-(\pm K)}]^T/\sqrt{2}$, with $K = (\beta + i\gamma/2)/\sqrt{\kappa^2 + (\beta + i\gamma/2)^2}$. In the two-dimensional (2D) parameter

 © 2022 American Physical Society

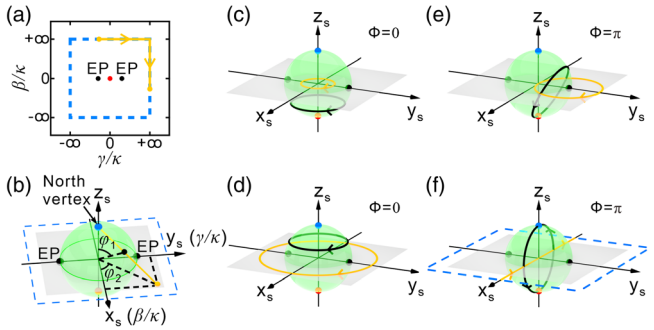

FIG. 1. (a) Hamiltonian parameter space described by $\zeta = (\beta/\kappa, \gamma/\kappa)$. The yellow line shows an evolution path along the parameter space boundary (blue dashed line). (b) RSP ($x_s^2 + y_s^2 + z_s^2 = 2^2$, $x_s = 2\sin\varphi_1\cos\varphi_2$, $y_s = 2\sin\varphi_1\sin\varphi_2$, and $z_s = 2\cos\varphi_1$) describing the Hamiltonian parameter space. (c)–(f) The evolution loops on RSP (black curves) and in the 2D parameter space (yellow curves) when encircling (c) no EP, (d) two EPs, and (e), (f) one EP. The loop in (f) locates in the center of the two EPs.

space $\zeta = (\beta/\kappa, \gamma/\kappa)$, the EPs are located at $\zeta = (0, 2)$ and $\zeta = (0, -2)$. When H approaches the points at infinity in ζ, i.e., $\beta/\kappa \to \pm\infty$ and/or $\gamma/\kappa \to \pm\infty$, the two eigenstates converge to $|\psi_1\rangle = [1, 0]^T$ and $|\psi_2\rangle = [0, 1]^T$, corresponding to E_1 and E_2 [$|\mathrm{Im}(E_1)| \leq |\mathrm{Im}(E_2)|$], respectively. The energy spectra form a self-intersecting RSU in ζ, and the topological features can be expressed as a Berry phase $\Phi = \pi$ when an EP is encircled twice with a quasidynamic approach [40]. The Berry phase around a path $\mathbf{C}$ can be defined as $\Phi = i\int_{\mathrm{C}} \langle\chi(\zeta)|\nabla_\zeta\psi(\zeta)\rangle d\zeta$, where $\langle\chi(\zeta)|$ is the left eigenstate and $\langle\chi(\zeta)|H = \langle\chi(\zeta)|E$, i.e., $H^\dagger|\chi(\zeta)\rangle = E^*|\chi(\zeta)\rangle$ [41–43]. Since H is a symmetric Hamiltonian according to Eq. (1), i.e., $H^T = H$, we have $H^\dagger = H^*$ and $|\chi(\zeta)\rangle = |\psi^*(\zeta)\rangle$. If the Hamiltonian evolves along the parameter space boundary [Fig. 1(a)], $\psi(\zeta)$ is constant, i.e., $|\nabla_\zeta\psi(\zeta)\rangle = 0$, which makes Φ equal to zero.

To present the trajectory induced by the infinite boundary, we can represent the full parameter space over a RSP of radius 2, as schematically shown in Fig. 1(b). The mapping procedure, called stereographic projection, is based on the following steps: first, the center of the sphere is aligned with the origin of the 2D parameter space as denoted in Fig. 1(a); then, the north pole (blue point on RSP) is connected to the yellow point in the 2D parameter space (gray plane) to form a line; last, its intersecting point with the RSP is the mapping point (black point). Here, we provide some examples to show connections between loops and its mapping counterparts. When the loop only encircles the origin of the parameter space, the mapping loop is in the southern hemisphere [Fig. 1(c)]; when the loop expands to include two EPs, the mapping loop is in the northern hemisphere [Fig. 1(d)]; and when the loop continues to expand and becomes the infinite boundary (blue dashed line), the mapping loop converges to the north vertex (blue point) [Fig. 1(b)]. The mapping operation can also be analytically expressed: we assume that the RSP radius is 2, and the mapping relation from the 2D parameter space to the RSP is $\beta/\kappa = 2\cot(\varphi_1/2)\cos(\varphi_2)$ and $\gamma/\kappa = 2\cot(\varphi_1/2)\sin(\varphi_2)$, where φ_1 is the polar angle and φ_2 is the azimuthal angle as denoted in Fig. 1(b). Since all the points on the parameter space boundaries with generally different loss rates are mapped onto the north vertex, the associated loss rate can be an arbitrary value (Supplemental Material [44], Note 1).

As a function of their Berry phase, encircling loops can be divided into two groups, characterized by $\Phi = 0$ and π. Encircling two EPs, as well as no EP, results in a Berry phase $\Phi = 0$. Therefore, the north vertex does not contribute to the Berry phase. In both cases, RSP is split by the loop into two surfaces, one containing two EPs and the other containing no EPs [Figs. 1(c) and 1(d)]. In contrast, encircling trajectories including one EP splits the RSP into two surfaces, each containing one EP [Figs. 1(e) and 1(f)] associated with a Berry phase $\Phi = \pi$. The former one in Fig. 1(e) does not pass through the infinite boundary, and therefore the trajectories on both RSP and real parameter space are closed. In the case of the latter one in Fig. 1(f), since the trajectory in real parameter space is blocked by the infinite boundary (dashed blue line), it is open. By mapping the infinite boundary with the same eigenstates onto the north vertex, we can achieve a closed mapping trajectory (black solid line) on the RSP. In this way, both mapping trajectories in Figs. 1(e) and 1(f) show their topological equivalence, since the closed loops encircle each one of the two EPs. On the RSP, it is not necessary to distinguish which EP is encircled, since the loop that encircles one EP shares the same Berry phase with the loop that encircles the other EP, i.e., they are topologically equivalent (Supplemental Material [44], Note 2).

The transmission loss accumulated along the mapping trajectory can be also interpreted from the perspective of RSP: the mapping trajectories in Figs. 1(e) and 1(f) encircle each of the two EPs simultaneously, and the distance relative to each EP located in the gain or loss region determines the transmission loss. The conventional mapping trajectory in Fig. 1(e) is close to the loss EP [$\zeta = (0, 2)$], associated with path-dependent loss along the entire path ($\gamma/\kappa > 0$), making the system prone to low transmittance. The loss difference between the two eigenstates causes the occurrence of nonadiabatic transitions (NATs), leading to an asymmetric response [11,12,45]. Instead, the mapping trajectory in Fig. 1(f), located in the middle of the two EPs, is not associated with any loss except at the north vertex, and hence it enables high-efficiency transmission. In Fig. 1(f), the NAT process is guaranteed by introducing a nonzero loss rate at the north vertex and exerting a sufficiently long evolution time to dissipate $|\psi_2\rangle$. See Supplemental Material [44], Note 3 for the evolution dynamics on how the loss affects the final

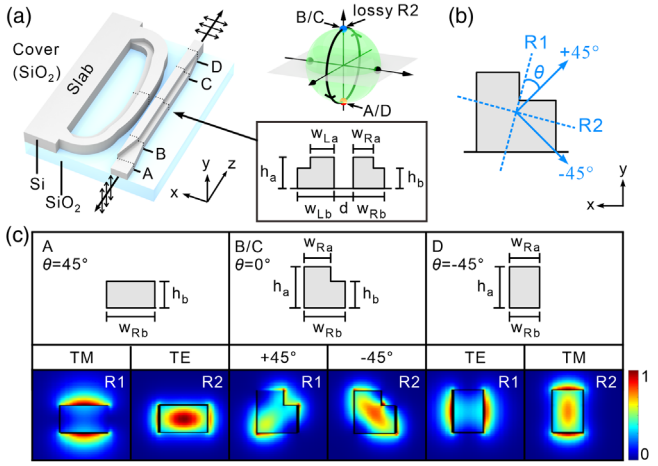

FIG. 2. (a) APLD made of silicon waveguides. The full height of the L-shaped waveguide is $h_a = 340$ nm, and the height of the lower waveguide is $h_b = 220$ nm. The width of the upper waveguide and the full waveguide is w_{La} (w_{Ra}) and w_{Lb} (w_{Rb}) for the left (right) waveguide, respectively. The gap separation between the two waveguides is d. (b) The polarization directions for $R1$ and $R2$ modes. (c) The cross sections of the right waveguide at A, B/C, and D, and their associated electric field intensity distributions for the R1 and R2 eigenmodes.

output states. Meanwhile, through the mapping of RSP we ensure that this loop indeed encircles each EP, leading to an asymmetric response. Thus, we simultaneously achieve both high efficiency and largely asymmetric transmission following this trajectory.

This specific trajectory can be mapped onto a suitably designed silicon waveguide tailored for APLD, as schematically depicted in Fig. 2(a). The right waveguide supports two orthogonal eigenmodes with different polarization directions, i.e., $R1$ ($|\psi_1\rangle$) and $R2$ ($|\psi_2\rangle$) modes with effective refractive indices n_{R1} and n_{R2} ($n_{R1} < n_{R2}$), respectively. θ represents the angle between the polarization direction of $R1$ and the $+45°$ axis [Fig. 2(b)]. In this configuration, the eigenmode in the right waveguide can be expressed as $|\psi\rangle = [A_1, A_2]^T$, in which A_1 and A_2 indicate the projection components of the normalized electric field amplitude along $+45°$ and $-45°$, respectively. Consequently, the Hamiltonian parameters in Eq. (1) can be expressed as $\beta = k_0(n_{R1} - n_{R2})(\sin^2\theta - \cos^2\theta)/2$, $\kappa = k_0(n_{R1} - n_{R2})\sin\theta\cos\theta$. γ is the loss rate exerted on the components of the electric field along $-45°$, and $k_0 = 2\pi/\lambda$ is the wave number, with λ being the wavelength (Supplemental Material [44], Note 4).

At the starting point A, the $R1$ mode is transverse magnetic (TM) polarized with $\theta = 45°$, corresponding to $\beta/\kappa = 0$ [Fig. 2(c)]. Between A and B, θ changes monotonically from 45° to 0°, reducing β/κ from 0 to $-\infty$, associated with the evolution path from A to B along the longitude on the RSP [illustration of Fig. 2(a)]. Between B and C, the right waveguide is axisymmetric along $+45°$ axis, so that R1 is polarized along $+45°$ direction with $\theta = 0°$, resulting in $\kappa = 0$ and $\beta/\kappa = \infty$ [Fig. 2(c)]. The left waveguide between B and C is designed to absorb the eigenmode polarized along the $-45°$ direction in the right waveguide via adiabatic coupling, associated with $\gamma > 0$. The whole evolution path between B and C takes place at the north vertex on the RSP. Between C and D, β/κ is varied monotonically from $+\infty$ to 0 as θ is reduced from 0° to $-45°$, and the Hamiltonian evolves from C to D along the longitude on the RSP. Although β, γ, and κ are finite, the Hamiltonian parameter space boundary is accessible based on the specifically tailored L-shaped waveguide.

Figures 3(a)–3(d) show the evolution trajectory of the system state on RSU (not RSP, mapped here with $\mathrm{atan}(E)/\kappa$ in the third dimension to cast it into a finite plot) for CW and ACW loops around the EP, where the CW and ACW loops correspond to light propagating along $+z$ and $-z$ in the right waveguide, respectively. The difference of the two eigenvalues is minimum at the EP, but both drastically change close to the EP [46]. In contrast, the difference of the two eigenvalues is maximum, but both tend to converge when approaching the infinity point. For the CW loop with $[1, 1]^T$ input, associated with the TE mode, $[1, 1]^T$ evolves to $[0, 1]^T$ when the Hamiltonian varies slowly from A to B [Fig. 3(a)]. Meanwhile, $[1, 0]^T$ is excited at B, due to the fact that rigorous adiabaticity cannot be fully guaranteed. During the NAT process from B to C, $[0, 1]^T$ is dissipated and $[1, 0]^T$ is preserved, making the dominant eigenstate of the system switch from $[0, 1]^T$ to $[1, 0]^T$. Finally, the Hamiltonian returns to the destination D with $[1, 1]^T$, and the corresponding output mode is TE. For the CW loop with $[1, -1]^T$ input [Fig. 3(b)], associated with the TM mode, the dominant eigenstate during the evolution is always lossless because a NAT does not occur, and the

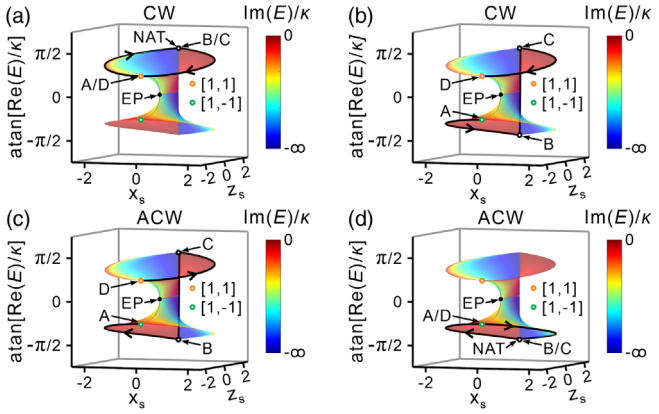

FIG. 3. (a) and (b) CW loops on RSU formed by the real part of the eigenvalues of H when the input state is (a) $[1, 1]^T$ and (b) $[1, -1]^T$. The RSU is extracted by casting the hemisphere with $y_s \geq 0$ (pure lossy case) of the RSP onto the x_s-z_s plane. The color of the surface indicates the imaginary part of the eigenvalues of H, in which a smaller imaginary part indicates a larger loss. (c) and (d) ACW loops when the input state is (c) $[1, 1]^T$ and (d) $[1, -1]^T$.

final output state is $[1,1]^T$, TE in nature. This indicates that the output mode for the CW direction is locked to TE, irrespective of the input mode. For the ACW loop [Figs. 3(c) and 3(d)], the output state is locked to $[1,-1]^T$, associated with TM polarization. The two sheets of RSU are self-intersecting, and the adiabatic evolution path between B and C is vertical, as the slope at B and C is infinite on this choice of RSU. A NAT occurs between B and C in Figs. 3(a) and 3(d), during which the evolution path switches from the blue to the red branch.

The L-shaped silicon waveguides shown in Fig. 2(a) are carefully tailored to map this evolution path by establishing the relation between structural parameters and the Hamiltonian parameters (Supplemental Material [44], Note 5). For the CW (ACW) loop with TE (TM) mode input to the right waveguide at A (D), the TE (TM) mode evolves to $R2$ polarized along $-45°$ at B (C) [Fig. 4(a)]. Meanwhile, $R1$ polarized along $+45°$ is excited because the length between A and B (D and C) is limited and the adiabatic evolution is not strictly satisfied. The device length between B and C is long enough so that $R2$ is fully absorbed by the left waveguide and the triggered $R1$ mode is retained, i.e., a NAT occurs. Finally, $R1$ evolves to TE (TM) from C to D (B to A) with a relatively low field intensity. For the CW (ACW) loop with TM (TE) input to the right waveguide at A (D), it evolves to $R1$ mode at B (C). The triggered $R2$ mode is absorbed between B and C, and $R1$ mode eventually evolves to TE (TM) mode from C to D (B to A).

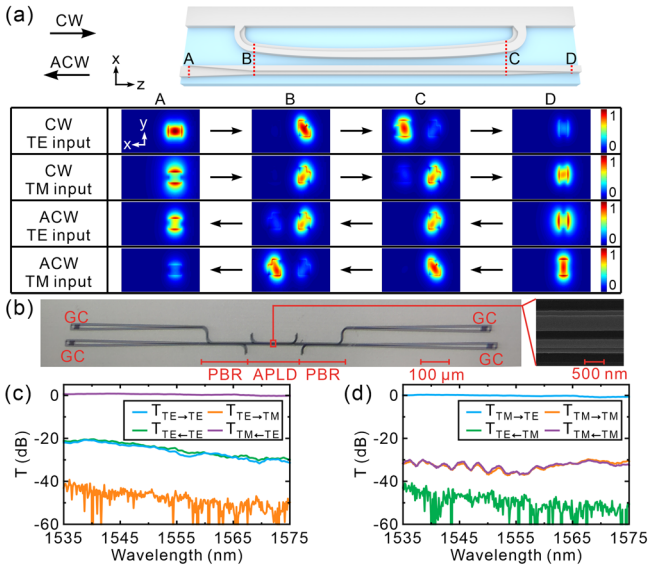

FIG. 4. (a) The cross-sectional electric field intensity distributions at A, B, C, and D. (b) Optical microscope images of the fabricated APLD, where the L-shaped waveguides are partially depicted by the SEM image on the right panel. (c),(d) Measured transmittance spectra over 1535–1575 nm wavelength range as (c) TE and (d) TM modes are injected, respectively.

Figure 4(b) shows the fabricated devices, with grating couplers (GCs), polarization beam splitter and rotators (PBRs) for measurement. The measured transmission efficiencies for TE and TM mode input are shown in Figs. 4(c) and 4(d), respectively (see Supplemental Material [44], Notes 6, 7 for the fabrication details and measurement scheme). $T_{P\to Q}$ ($T_{P\leftarrow Q}$) represents the transmission efficiency of Q mode from the output port for input P mode from the left (right) port (P or Q mode refer to TE or TM mode). For a left-side input, $T_{\mathrm{TE}\to\mathrm{TE}} \gg T_{\mathrm{TE}\to\mathrm{TM}}$ and $T_{\mathrm{TM}\to\mathrm{TE}} \gg T_{\mathrm{TM}\to\mathrm{TM}}$, indicating that the output mode is locked to TE. For right-side excitation, $T_{\mathrm{TM}\leftarrow\mathrm{TE}} \gg T_{\mathrm{TE}\leftarrow\mathrm{TE}}$ and $T_{\mathrm{TM}\leftarrow\mathrm{TM}} \gg T_{\mathrm{TE}\leftarrow\mathrm{TM}}$, indicating that the output mode is locked to TM. It can be observed that $T_{\mathrm{TM}\to\mathrm{TE}}$ and $T_{\mathrm{TM}\leftarrow\mathrm{TE}}$ are close to 100% around 1550 nm. The mode crosstalk is defined as the energy ratio of the undesired mode to total output [47]. The mode crosstalks TM → TE, TM ← TE, and TE → TE are all below −20 dB, while TM ← TM is below −10 dB. The experimental results well validate the asymmetric polarization-locked performance. It should be noted that the APLD is sensitive to the alignment error, and therefore the alignment should be carefully controlled in fabrication (Supplemental Material [44], Note 8).

Here, we can also treat the APLD as a three-section optical system (Supplemental Material [44], Note 9). The AB/CD section is used as a leaky polarization controller that converts the input mode into the dominant eigenmode and its orthogonal eigenmode. The BC section serves as a selective optical attenuator that takes away one of the eigenmodes. The approach of using a three-section optical system can also be extended to develop asymmetrical polarization conversion devices for spatial light [48]. These alternative schemes, however, are limited in terms of operational bandwidth. EP encircling on the contrary ensures large working bandwidths, due to adiabatic parameter evolution of the energy spectra [8,15,20]. Our simulations predict that the practical bandwidth of the described operation can be as large as the entire range 1450–1750 nm (Supplemental Material [44], Note 10). The presented Riemann-encircling strategy can be extended to study asymmetrical state-locked response in a multistate non-Hermitian system (Supplemental Material [44], Note 11].

In conclusion, we have shown that dynamically encircling an EP on RSP can enable asymmetric polarization conversion, and a continuous encircling trajectory passing through the north vertex can realize near-unity asymmetric transmission. We experimentally demonstrated nearly 100% asymmetric polarization conversion between TE and TM modes with mode crosstalk below −20 dB at 1550 nm in silicon waveguides. These results enable the practical realization of highly efficient gain-free, broadband asymmetric polarization conversion on chip, and hold the promise for new opportunities for optical devices and applications.

This work has been supported by National Natural Science Foundation of China (Grant No. 12074137), National Key Research and Development Project of China (Grant No. 2021YFB2801903), State Key Laboratory of Artificial Microstructure & Mesoscopic Physics (Peking University), State Key Laboratory of Advanced Technology for Materials Synthesis and Processing (Wuhan University of Technology), Air Force Office of Scientific Research MURI program, and the Simons Foundation. We thank Pan Li in the Center of Micro-Fabrication and Characterization (CMFC) of WNLO for the support in plasma enhanced chemical vapor deposition, and Jun Su in the Center of Micro-Fabrication and Characterization of WNLO for the support in SEM test.

The authors declare that they have no competing interests.

*These authors contributed equally to this work.
†Corresponding author.
chen.lin@mail.hust.edu.cn

[1] H. Hodaei, A. U. Hassan, S. Wittek, H. Garcia-Gracia, R. El-Ganainy, D. N. Christodoulides, and M. Khajavikhan, Nature (London) **548**, 187 (2017).
[2] W. Chen, S. Kaya Ozdemir, G. Zhao, J. Wiersig, and L. Yang, Nature (London) **548**, 192 (2017).
[3] J.-H. Park, A. Ndao, W. Cai, L. Hsu, A. Kodigala, T. Lepetit, Y.-H. Lo, and B. Kanté, Nat. Phys. **16**, 462 (2020).
[4] Z. Lin, H. Ramezani, T. Eichelkraut, T. Kottos, H. Cao, and D. N. Christodoulides, Phys. Rev. Lett. **106**, 213901 (2011).
[5] L. Feng, Y. L. Xu, W. S. Fegadolli, M. H. Lu, J. E. Oliveira, V. R. Almeida, Y. F. Chen, and A. Scherer, Nat. Mater. **12**, 108 (2013).
[6] H. Zhao, X. Qiao, T. Wu, B. Midya, S. Longhi, and L. Feng, Science **365**, 1163 (2019).
[7] W. Song, W. Sun, C. Chen, Q. Song, S. Xiao, S. Zhu, and T. Li, Phys. Rev. Lett. **123**, 165701 (2019).
[8] J. Doppler, A. A. Mailybaev, J. Bohm, U. Kuhl, A. Girschik, F. Libisch, T. J. Milburn, P. Rabl, N. Moiseyev, and S. Rotter, Nature (London) **537**, 76 (2016).
[9] S. N. Ghosh and Y. D. Chong, Sci. Rep. **6**, 19837 (2016).
[10] A. U. Hassan, B. Zhen, M. Soljacic, M. Khajavikhan, and D. N. Christodoulides, Phys. Rev. Lett. **118**, 093002 (2017).
[11] X.-L. Zhang, T. Jiang, and C. T. Chan, Light Sci. Appl. **8**, 88 (2019).
[12] X.-L. Zhang, S. Wang, B. Hou, and C. T. Chan, Phys. Rev. X **8**, 021066 (2018).
[13] X.-L. Zhang and C. T. Chan, Commun. Phys. **2**, 63 (2019).
[14] Q. Liu, S. Li, B. Wang, S. Ke, C. Qin, K. Wang, W. Liu, D. Gao, P. Berini, and P. Lu, Phys. Rev. Lett. **124**, 153903 (2020).
[15] A. Li, J. Dong, J. Wang, Z. Cheng, J. S. Ho, D. Zhang, J. Wen, X.-L. Zhang, C. T. Chan, A. Alù, C.-W. Qiu, and L. Chen, Phys. Rev. Lett. **125**, 187403 (2020).
[16] A. Guo, G. J. Salamo, D. Duchesne, R. Morandotti, M. Volatier-Ravat, V. Aimez, G. A. Siviloglou, and D. N. Christodoulides, Phys. Rev. Lett. **103**, 093902 (2009).
[17] M. Lawrence, N. Xu, X. Zhang, L. Cong, J. Han, W. Zhang, and S. Zhang, Phys. Rev. Lett. **113**, 093901 (2014).
[18] B. Peng, Ş. K. Özdemir, M. Liertzer, W. Chen, J. Kramer, H. Yılmaz, J. Wiersig, S. Rotter, and L. Yang, Proc. Natl. Acad. Sci. U.S.A. **113**, 6845 (2016).
[19] L. Feng, R. El-Ganainy, and L. Ge, Nat. Photonics **11**, 752 (2017).
[20] J. W. Yoon, Y. Choi, C. Hahn, G. Kim, S. H. Song, K. Y. Yang, J. Y. Lee, Y. Kim, C. S. Lee, J. K. Shin, H. S. Lee, and P. Berini, Nature (London) **562**, 86 (2018).
[21] M. P. Hokmabadi, A. Schumer, D. N. Christodoulides, and M. Khajavikhan, Nature (London) **576**, 70 (2019).
[22] Y.-H. Lai, Y.-K. Lu, M.-G. Suh, Z. Yuan, and K. Vahala, Nature (London) **576**, 65 (2019).
[23] M.-A. Miri and A. Alù, Science **363**, eaar7709 (2019).
[24] A. L. M. Muniz, M. Wimmer, A. Bisianov, U. Peschel, R. Morandotti, P. S. Jung, and D. N. Christodoulides, Phys. Rev. Lett. **123**, 253903 (2019).
[25] S. Xia, D. Kaltsas, D. Song, I. Komis, J. Xu, A. Szameit, H. Buljan, K. G. Makris, and Z. Chen, Science **372**, 72 (2021).
[26] Z. Chen and M. Segev, eLight **1**, 2 (2021).
[27] K. Ding, G. Ma, Z. Q. Zhang, and C. T. Chan, Phys. Rev. Lett. **121**, 085702 (2018).
[28] W. Tang, X. Jiang, K. Ding, Y.-X. Xiao, Z.-Q. Zhang, C. T. Chan, and G. Ma, Science **370**, 1077 (2020).
[29] H.-Z. Chen, T. Liu, H.-Y. Luan, R.-J. Liu, X.-Y. Wang, X.-F. Zhu, Y.-B. Li, Z.-M. Gu, S.-J. Liang, H. Gao, L. Lu, L. Ge, S. Zhang, J. Zhu, and R.-M. Ma, Nat. Phys. **16**, 571 (2020).
[30] Y. Li, Y.-G. Peng, L. Han, M.-A. Miri, W. Li, M. Xiao, X.-F. Zhu, J. Zhao, A. Alù, S. Fan, and C.-W. Qiu, Science **364**, 170 (2019).
[31] Z. Dong, Z. Li, F. Yang, C.-W. Qiu, and J. S. Ho, National electronics review **2**, 335 (2019).
[32] L. Shao, W. Mao, S. Maity, N. Sinclair, Y. Hu, L. Yang, and M. Lončar, National electronics review **3**, 267 (2020).
[33] F. Klauck, L. Teuber, M. Ornigotti, M. Heinrich, S. Scheel, and A. Szameit, Nat. Photonics **13**, 883 (2019).
[34] C. Dembowski, B. Dietz, H. D. Gräf, H. L. Harney, A. Heine, W. D. Heiss, and A. Richter, Phys. Rev. E **69**, 056216 (2004).
[35] F. Yu, X.-L. Zhang, Z.-N. Tian, Q.-D. Chen, and H.-B. Sun, Phys. Rev. Lett. **127**, 253901 (2021).
[36] Y. Choi, C. Hahn, J. W. Yoon, S. H. Song, and P. Berini, Nat. Commun. **8**, 14154 (2017).
[37] X.-L. Zhang, J.-F. Song, C. T. Chan, and H.-B. Sun, Phys. Rev. A **99**, 063831 (2019).
[38] G. Lopez-Galmiche, H. E. Lopez Aviles, A. U. Hassan, A. Schumer, T. Kottos, P. L. LiKamWa, M. Khajavikhan, and D. N. Christodoulides, Omnipolarizer action via encirclement of exceptional points, *Conference on Lasers and Electro-Optics* (Optical Society of America, Washington, DC, 2020), pp. FM1A.3.
[39] S. S. Aleshkina, A. Fedotov, D. Korobko, D. Stoliarov, D. S. Lipatov, V. V. Velmiskin, V. L. Temyanko, L. V. Kotov, R. Gumenyuk, and M. E. Likhachev, Opt. Lett. **45**, 2275 (2020).
[40] T. Gao, E. Estrecho, K. Y. Bliokh, T. C. H. Liew, M. D. Fraser, S. Brodbeck, M. Kamp, C. Schneider, S. Höfling, Y. Yamamoto, F. Nori, Y. S. Kivshar, A. G. Truscott, R. G. Dall, and E. A. Ostrovskaya, Nature (London) **526**, 554 (2015).
[41] M. V. Berry, Proc. R. Soc. A **392**, 45 (1984).

[42] F. Keck, H. J. Korsch, and S. Mossmann, J. Phys. A **36**, 2125 (2003).
[43] S.-D. Liang and G.-Y. Huang, Phys. Rev. A **87**, 012118 (2013).
[44] See Supplemental Material at http://link.aps.org/supplemental/10.1103/PhysRevLett.129.127401 for more details on imaginary part of the eigenvalues, evolution dynamics with different losses, Schrödinger-type equation for the *L*-shaped waveguide, structural parameters, fabrication process, measurement scheme, alignment error analysis, asymmetric polarization conversion, simulation results, and asymmetric state-locked response in an *N*-state system.
[45] A. U. Hassan, G. L. Galmiche, G. Harari, P. LiKamWa, M. Khajavikhan, M. Segev, and D. N. Christodoulides, Phys. Rev. A **96**, 052129 (2017).
[46] A. Lupu, V. V. Konotop, and H. Benisty, Sci. Rep. **7**, 13299 (2017).
[47] L.-W. Luo, N. Ophir, C. P. Chen, L. H. Gabrielli, C. B. Poitras, K. Bergmen, and M. Lipson, Nat. Commun. **5**, 3069 (2014).
[48] J. B. Khurgin, Y. Sebbag, E. Edrei, R. Zektzer, K. Shastri, U. Levy, and F. Monticone, Optica **8**, 563 (2021).

Correction: The omission of an email address byline footnote for the seventh author has been fixed.